The Metal Centers of Particulate Methane Monooxygenase from *Methylosinus trichosporium* OB3b[†,‡]

Amanda S. Hakemian,[§] Kalyan C. Kondapalli,[||] Joshua Telser,[§,⊥] Brian M. Hoffman,[§] Timothy L. Stemmler,*[,||] and Amy C. Rosenzweig*[,§]

Departments of Biochemistry, Molecular Biology, and Cell Biology and of Chemistry, Northwestern University, Evanston, Illinois 60208, and Department of Biochemistry and Molecular Biology, Wayne State University School of Medicine, Detroit, Michigan 48201

Received April 4, 2008; Revised Manuscript Received May 8, 2008

ABSTRACT: Particulate methane monooxygenase (pMMO) is a membrane-bound metalloenzyme that oxidizes methane to methanol in methanotrophic bacteria. The nature of the pMMO active site and the overall metal content are controversial, with spectroscopic and crystallographic data suggesting the presence of a mononuclear copper center, a dinuclear copper center, a trinuclear center, and a diiron center or combinations thereof. Most studies have focused on pMMO from *Methylococcus capsulatus* (Bath). pMMO from a second organism, *Methylosinus trichosporium* OB3b, has been purified and characterized by spectroscopic and crystallographic methods. Purified *M. trichosporium* OB3b pMMO contains ~2 copper ions per 100 kDa protomer. Electron paramagnetic resonance (EPR) spectroscopic parameters indicate that type 2 Cu(II) is present as two distinct species. Extended X-ray absorption fine structure (EXAFS) data are best fit with oxygen/nitrogen ligands and reveal a Cu−Cu interaction at 2.52 Å. Correspondingly, X-ray crystallography of *M. trichosporium* OB3b pMMO shows a dinuclear copper center, similar to that observed previously in the crystal structure of *M. capsulatus* (Bath) pMMO. There are, however, significant differences between the pMMO structures from the two organisms. A mononuclear copper center present in *M. capsulatus* (Bath) pMMO is absent in *M. trichosporium* OB3b pMMO, whereas a metal center occupied by zinc in the *M. capsulatus* (Bath) pMMO structure is occupied by copper in *M. trichosporium* OB3b pMMO. These findings extend previous work on pMMO from *M. capsulatus* (Bath) and provide new insight into the functional importance of the different metal centers.

Methanotrophs are eubacteria capable of utilizing methane as their only carbon and energy source. Methanotrophs are divided into several classes on the basis of their cell morphologies, membrane arrangements, and pathways for carbon assimilation. The two most widely studied organisms are the type X methanotroph *Methylococcus capsulatus* (Bath) and the type II methanotroph *Methylosinus trichosporium* OB3b (*1*). The first step of their metabolic pathway is the conversion of methane to methanol by the enzyme methane monooxygenase (MMO),[1] which exists in both a well-studied, but rarely expressed, soluble iron-containing form (sMMO) (*2*) and a membrane-bound particulate form (pMMO) (*2, 3*). Although the active site and chemistry of sMMO are well established, the nature of the pMMO catalytic center remains controversial, particularly regarding the number and types of metal ions present.

pMMO comprises three subunits: pmoB or α (47 kDa), pmoA or β (24 kDa), and pmoC or γ (22 kDa). Several laboratories have reported that purified *M. capsulatus* (Bath) pMMO contains 2−3 copper ions per 100 kDa αβγ protomer (*4–6*). Similarly, *M. trichosporium* OB3b pMMO was found to contain 2 copper ions per αβγ protomer (*7*). By contrast, Chan and co-workers have reported 15−20 copper ions per *M. capsulatus* (Bath) pMMO protomer (*8, 9*). This large number of copper ions is proposed to be arranged in trinuclear clusters based on the interpretation of a broad isotropic electron paramagnetic resonance (EPR) signal at $g \sim 2.1$ and on redox potentiometric studies (*10, 11*). However, other investigators observe only a type 2 Cu(II) EPR signal for pMMO from several different organisms (*3–6, 12, 13*). The iron content of pMMO is also contentious. Samples of iron-free pMMO have been obtained from both *M. capsulatus* (Bath) (*9*) and *M. trichosporium* OB3b (*7*). Other preparations of *M. capsulatus* (Bath) pMMO contain 0.75−2.5 iron ions per 100 kDa (*4–6, 13*).

[†] This work was supported by National Institutes of Health Grants HL13531 (to B.M.H.), DK068139 (to T.L.S.), and GM070473 (to A.C.R.). A.S.H. was the recipient of an NSF graduate research fellowship.

[‡] The coordinates of *Methylosinus trichosporium* OB3b pMMO have been deposited in the Protein Data Bank with accession code 3CHX.

* To whom correspondence may be addressed. A.C.R.: tel, 847-467-5301; fax, 847-467-6489; e-mail, amyr@northwestern.edu. T.L.S.: tel, 313-577-5712; fax, 313-577-2765; e-mail, tstemmle@med.wayne.edu.

[§] Northwestern University.

[||] Wayne State University School of Medicine.

[⊥] Permanent address: Department of Biological, Chemical and Physical Sciences, Roosevelt University, Chicago, IL 60605.

[1] Abbreviations: MMO, methane monooxygenase; sMMO, soluble methane monooxygenase; pMMO, particulate methane monooxygenase; EPR, electron paramagnetic resonance; PIPES, piperazine-1,4-bis(2-ethanesulfonic acid); DDM, dodecyl β-D-maltoside; Tris, tris(hydroxymethyl)aminomethane; XAS, X-ray absorption spectroscopy; EXAFS, extended X-ray absorption fine structure; UDM, undecyl β-D-maltoside.

10.1021/bi800598h CCC: $40.75
Published on Web 06/10/2008

The crystal structure of *M. capsulatus* (Bath) pMMO revealed that pMMO is an $\alpha_3\beta_3\gamma_3$ trimer, of which each $\alpha\beta\gamma$ protomer houses three metal centers (*14, 15*). Two of the metal centers in the structure contain copper: a dinuclear copper center for which the three histidine ligands are strictly conserved and a mononuclear copper center that includes two histidine ligands, of which one is not conserved in other pMMOs and the related ammonia monooxygenase (*3*). The third metal site, composed of strictly conserved ligands, is occupied by a zinc ion in the crystal structure, most likely derived from the crystallization buffer. The physiological metal content of this site is unknown. One possibility is a diiron center (*14*), and recent Mössbauer spectroscopic data suggest that this model is plausible (*16*). Additional metal binding sites depleted during crystallization may exist as well, and a potential transmembrane metal binding site identified in the crystal structure (*14*) has been proposed to house a tricopper cluster (*10*). To further investigate the composition and functional relevance of the pMMO metal centers, we have isolated pMMO from *M. trichosporium* OB3b. Spectroscopic and crystallographic characterization of *M. trichosporium* OB3b pMMO complements previous work on *M. capsulatus* (Bath) pMMO and directly addresses questions about the metal centers raised by the *M. capsulatus* (Bath) pMMO crystal structure.

MATERIALS AND METHODS

Bacterial Growth. M. trichosporium OB3b cultures were obtained from the laboratories of Jeremy Semrau (University of Michigan) and John Lipscomb (University of Minnesota). Fermentations were conducted in a 15 L bioreactor (New Brunswick Scientific, Edison, NJ) using previously described culture media (*17*) with the addition of 50 μM copper sulfate. Cells were grown at 30 °C and an agitation rate of 300−400 rpm and were purged with a 3:1 methane/air mixture at 1.2−1.6 L/min total gas flow. The pH in the fermentor was maintained at 7.0 by addition of 1 N NaOH (aq) and 1 N H_2SO_4 (aq). Cells were harvested at an OD_{600} between 6.0 and 10.0, and typically 2 L was retained in the bioreactor, and sterile media were added to start another growth. Harvested cells were centrifuged at 3000*g* for 20 min, washed three times with 10 mM PIPES, pH 7.0, frozen in liquid nitrogen, and stored at −80 °C.

Membrane Isolation and Protein Purification. Cells were suspended in lysis buffer (25 mM PIPES, pH 7.0, and 250 mM NaCl) supplemented with 500 μM $CuSO_4$, which was degassed on a vacuum line and back-filled with argon gas prior to use. After lysis by sonication, cell debris was removed by centrifugation at 24000*g* for 2 h. The membrane fraction was isolated by ultracentrifugation for 1 h at 160000*g*. Membranes were rinsed twice with lysis buffer using a Dounce homogenizer for resuspension. After the final wash, membranes were resuspended in lysis buffer to a concentration of ~20 mg/mL and frozen in liquid nitrogen. Membrane aliquots were stored at −80 °C until needed.

For solubilization, 1.5 mg of dodecyl β-D-maltoside (DDM, Anatrace, Maumee, OH) was added to the membranes for every 1 mg of protein, usually as a stock of 100 mg/mL DDM but sometimes as a solid (usually only for large samples). The protein concentration of the membrane sample was measured using the D_c assay (Bio-Rad Laboratories, Richmond, CA). The sample was incubated with the detergent, gently rocking or stirring at 4 °C for ~15 min. Before loading onto a Source 15Q (GE Healthcare, Piscataway, NJ) anion-exchange column, solubilized membranes were diluted 4- or 5-fold with buffer A (50 mM Tris, pH 8.5, 0.5% (w/v) DDM), degassed as described above. After the protein was loaded onto the column and rinsed with two column volumes of buffer A, pMMO was eluted with a 0−50% gradient of degassed buffer B (50 mM Tris, pH 8.5, 2 M NaCl, 0.5% (w/v) DDM). During the column run, the buffers were kept anaerobic by suspending balloons filled with argon gas above the bottles. Purified pMMO was concentrated to ~20 mg/mL with either a Centriprep 50 for large volumes or a Microcon YM-100 for smaller volumes (Millipore Corp., Billerica, MA). Concentrations of purified pMMO were determined by using an extinction coefficient (253511 M^{-1} cm^{-1} per 100 kDa enzyme) determined by amino acid analysis (Protein Chemistry Laboratory, Texas A&M University, College Station, TX). A representative SDS−PAGE gel of purified pMMO is shown in Figure 1.

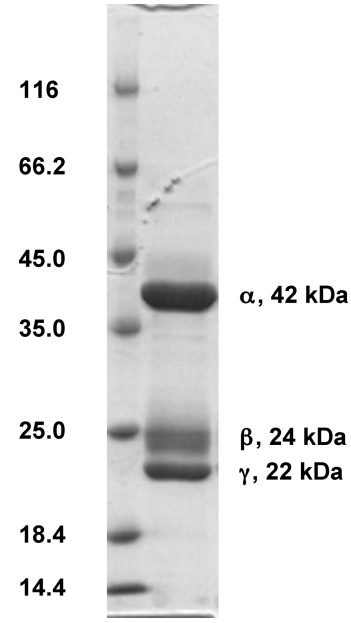

FIGURE 1: SDS−PAGE gel of purified *M. trichosporium* OB3b pMMO (30 μg). Molecular mass standards and pMMO subunits are labeled.

Activity Assays and Metal Analysis. The activity of pMMO at 30 °C was measured by monitoring the epoxidation of propylene (*6, 18*) with duroquinol as a reductant (*6*). After being shaken at 30 °C for 3 min, the propylene oxide product was detected by gas chromatography using a Hewlett-Packard 5890 gas chromatograph equipped with a Porapak Q column (6 ft × 1/8 in., Supelco, Bellafonte, PA) and quantified by comparison with propylene oxide standard (Sigma Aldrich, St. Louis, MO). Before the activity of purified pMMO was measured, samples were exchanged into lysis buffer containing 0.05% (w/v) Brij-58 (Anatrace, Maumee, OH). All assays were performed in at least duplicate. Metal contents were determined by inductively coupled plasma−optical emission spectroscopy (ICP-OES) using a Varian Vista-MPX CCD simultaneous ICP-OES. Standards were prepared by diluting copper, zinc, or iron atomic absorption standards (Sigma Aldrich, St. Louis, MO) with 2% (v/v) trace metal grade nitric acid (Fisher Scientific,

Pittsburgh, PA) using acid-rinsed volumetric glassware. pMMO samples were diluted to a concentration of ~0.2 mg/mL in 2% (v/v) trace metal grade nitric acid using acid-rinsed volumetric glassware prior to analysis. All measurements were made in triplicate, and two or more independent samples were analyzed.

EPR Spectroscopy. Samples of purified pMMO for EPR were prepared as described above except for the inclusion of 10% (v/v) glycerol in the final samples. EPR spectra were recorded on a highly modified Bruker ESP 300. Samples were kept frozen using a finger Dewar filled with liquid nitrogen. A 500 μM aqueous solution of CuEDTA was used as a standard, and EPR spectra of all samples were recorded under identical conditions as those for the standard. The spectra were background corrected by subtraction of a spectrum for buffer recorded under identical conditions. Double integration of background-corrected spectra was performed digitally using LabCalc software. The same field integration range was used for all samples, and the spectra were baseline-corrected (linear) after the first digital integration. The combined error of EPR quantitation and measurement of protein and copper content is ~±20%. EPR simulations were performed using the program QPOWA, originally written by Belford and co-workers (*19, 20*) and subsequently modified by J. Telser.

XAS Spectroscopy. Two independent pMMO samples were prepared for XAS studies in 50 mM Tris, pH 8.5, 0.5% (w/v) DDM, 250 mM NaCl, and 30% (v/v) glycerol at Cu concentrations between 1 and 2 mM. Samples were loaded into Lucite cells, wrapped with Kapton tape, flash frozen in liquid nitrogen, and stored at −80 °C until data collection. XAS data were collected at the Stanford Synchrotron Radiation Laboratory (SSRL) on beamline 10-2 and at the National Synchrotron Light Source (NSLS) on beamline X9-b. The SSRL beamline was equipped with a Si[220] double crystal monochromator while the NSLS beamline utilized a Si[111] monochromator; both beamlines were equipped with harmonic rejection mirrors. During data collection, samples were maintained at 10 K using an Oxford Instruments continuous-flow liquid helium cryostat at SSRL and at 24 K using a He Displex Cryostat at NSLS. Protein fluorescence−excitation spectra were collected using 13-element Ge solid-state detectors at both beamlines. At SSRL, a 0.6 μm nickel filter and Soller slits were placed between the cryostat and detector to filter background fluorescence scattering. XAS spectra at both facilities were measured in 5 eV increments in the pre-edge region (8750−8960 eV), 0.25 eV increments in the edge region (8986−9050 eV), and 0.05 Å^{-1} increments in the extended X-ray absorption fine structure (EXAFS) region (to k = 13.5 Å^{-1} Cu), integrating from 1 to 20 s in a k^3 weighted manner for a total scan length of approximately 40 min. X-ray energies were individually calibrated by collecting Cu foil absorption spectra simultaneously with protein data. The first inflection point of the Cu foil spectrum was assigned to 8980.3 eV. Each fluorescence channel of each scan was examined for spectral anomalies prior to averaging, and spectra were closely monitored for photoreduction. SSRL data represent the average of six to seven scans while NSLS data represent the average of nine to ten scans.

XAS data were processed using the Macintosh OS X version of the EXAFSPAK program suite (*21*) integrated with the Feff v8 software (*22*) for theoretical model generation. Data reduction utilized a Gaussian function in the pre-edge region and a three-region cubic spline throughout the EXAFS region. Data were converted to k-space using a copper E_0 value of 9000 eV. The k cubed weighted EXAFS was truncated at 1.0 and 12.85 Å^{-1} for filtering purposes. This k range corresponds to a spectral resolution of ca. 0.14 Å for all copper−ligand interactions; therefore, only independent scattering environments outside 0.14 Å were considered resolvable in the EXAFS fitting analysis (*23*). EXAFS fitting analysis was performed on raw/unfiltered data. EXAFS data were fit using both single and multiple scattering amplitude and phase functions calculated with the program Feff v8. Single scattering theoretical models were calculated for carbon, oxygen, sulfur, and copper coordination to simulate copper−nearest neighbor ligand environments. A multiple scattering Cu−imidazole theoretical model was calculated to simulate the numerous scattering interactions observed from the linear ring. Scale factors (Sc) and E_0 values used during the simulations were calibrated by fitting crystallographically characterized copper models at different metal oxidation states, as described elsewhere (*24*). Criteria for judging the best-fit simulation utilized both the lowest mean square deviation between data and fit (F'), corrected for the number of degrees of freedom (*25*), and a reasonable Debye−Waller factor (σ^2 < 0.006 Å^2).

Crystallization and Structure Determination. For crystallization, purified *M. trichosporium* OB3b pMMO was exchanged into an appropriate buffer, usually 50 mM Tris, pH 8.5, and 0.03% (w/v) undecyl β-D-maltoside (UDM, Anatrace), by diluting and concentrating with a Microcon YM-100 three times. An initial crystallization condition was identified with the Wizard II screen (Emerald BioSystems, Bainbridge Island, WA) and optimized. Crystals were grown using sitting-drop geometry at room temperature. Drops contained 1 μL of 18−22 mg/mL purified pMMO and 1 μL of precipitant solution (100 mM cacodylate, pH 6.5, 20% (v/v) PEG 3000, 250 mM magnesium formate or manganese chloride). Unlike *M. capsulatus* (Bath) pMMO (*14*), zinc is not required for crystallization. Crystals grew within 2 weeks, but crystals harvested after 3−6 months resulted in the best diffraction. Crystals that diffracted beyond 10 Å resolution had dimensions 1.0 × 0.25 × 0.25 mm^3, but most crystals were smaller and not useful for data collection. Crystals were flash frozen using 25% (v/v) PEG 400, 75 mM cacodylate, pH 6.5, 15% (v/v) PEG 3000, and 187.5 mM magnesium formate (crystal pmmo17 in Table 1) or manganese chloride (crystal pmmo08 in Table 1) as a cryoprotectant. The crystals belong to space group $P2_12_12_1$. The unit cell dimensions varied from crystal to crystal (Table 1).

All data sets were collected at the GM/CA-CAT beamline at the Advanced Photon Source (Argonne National Laboratory, Argonne, IL) with a MarMosaic300 detector and processed with XDS (*26*) or MOSFLM (*27*) and SCALA (*28*) (Table 1). The structure was solved to 3.9 Å resolution by molecular replacement with PHASER (*29*) using the *M. capsulatus* (Bath) pMMO trimer (*14*) (accession code 1YEW) as a search model. The sequence was changed to that of *M. trichosporium* OB3b by threading the sequences (NCBI accession numbers AAA87220 (PmoA), AAF37894 (PmoB), AAF37893 (PmoC)) onto the molecular replacement model using Swiss-PdbViewer (*30*). The programs Coot (*31*)

Table 1: Data Collection and Refinement Statistics[a]

	pmmo17	pmmo17_aniso	pmmo08_3Cu	pmmo08_3Zn
		Data Collection		
space group	$P2_12_12_1$		$P2_12_12_1$	
cell dimensions, *a*, *b*, *c* (Å)	113.8, 184.1, 203.9		117.4, 184.7, 192.3	
wavelength (Å)	0.979	0.979	1.378	1.278
resolution (Å)	38−3.90 (4.10−3.90)	38−2.91 (3.05−2.91)	40.0−4.30 (4.52−4.30)	40.0−5.50 (5.80−5.50)
R_{sym}[b,c]	0.086 (37.6)		0.079 (0.351)	0.067 (0.293)
$I/\sigma I$	7.5 (2.0)	8.0 (5.5)	4.1 (1.8)	4.0 (1.9)
completeness (%)[b]	99.8 (99.8)	59.7 (4.5)	97.9 (99.2)	98.1 (99.2)
redundancy	7.4		3.5	3.4
		Refinement		
resolution (Å)	38−3.90	38−2.91	40−4.30	
no. of reflections	39693	56495	54183	
R_{work}[d]/R_{free}[e]	0.342/0.377	0.365/0.408	0.344/0.388	
no. of protein atoms	18945		18945	
no. of Cu atoms	9		9	
average *B*-factor	148.8		166.6	
rmsd, bond lengths (Å)	0.011		0.010	
rmsd, bond angles (deg)	1.864		1.679	

[a] pmmo17 and pmmo08 refer to two different crystals. [b] $R_{sym} = \sum|I_{obs} - I_{av}|/\sum F_{obs}$, where the summation is over all reflections. [c] Values in parentheses refer to the highest resolution shell. [d] $R_{work} = \sum|F_o - F_c|/\sum F_o$. [e] For calculation of R_{free}, 5% of the reflections were reserved.

Table 2: Metal Analysis of *M. trichosporium* OB3b pMMO

	Cu per 100 kDa	EPR-detectable Cu (%)	Zn per 100 kDa	Fe per 100 kDa
membrane-bound	4.8 ± 1.1	97 ± 6	2.7 (±1.8) × 10^{-3}	2.1 (±0.8) × 10^{-2}
solubilized	4.0 ± 1.1	96 ± 24	5.5 (±0.5) × 10^{-3}	3.4 (±1.2) × 10^{-2}
purified	1.4 ± 0.6	86 ± 9	1.3 (±0.6)× 10^{-3}	7.6 (±6.3) × 10^{-5}

and CNS (*32*) were used for model building and refinement. Strict NCS restraints were imposed between the three protomers throughout the refinement, and composite omit maps were used for validation. Data were additionally processed using the Diffraction Anisotropy Server (*33*) which allowed the inclusion of some data to 2.9 Å resolution (Table 1). Although the higher resolution shells are very incomplete, the anisotropically scaled data did reveal density for some side chains not present in the 3.9 Å maps. The final model consists of residues 40−283, 295−317, 328−346, and 351−426 for pmoB, 12−249 for pmoA, and 18−176 for pmoC, 3 copper ions modeled on the basis of anomalous Fourier maps (vide infra), and 47 additional alanine residues per protomer. A Ramachandran plot generated with PROCHECK (*34*) indicates good geometry with 92.1% of the residues in the most favored and additionally allowed regions. Because native crystals were not isomorphous, molecular replacement with PHASER (*29*) and refinement were carried out independently for data sets collected from different crystals (Table 1).

RESULTS AND DISCUSSION

Metal Content and Activity. The membrane-bound pMMO contains 4.8 ± 1.1 copper ions per 100 kDa protomer, and a similar stoichiometry of 4.0 ± 1.1 is obtained after solubilization (Table 2). By contrast, many preparations of membrane-bound and solubilized *M. capsulatus* (Bath) pMMO contain 15−20 copper ions per protomer (*6, 9, 35*). Initial reports for *M. trichosporium* OB3b membrane-bound pMMO indicated the presence of approximately 10 copper ions per 100 kDa (*36, 37*). Upon purification, the copper content is reduced to 1.4 ± 0.6 copper ions per protomer (Table 2). Early samples purified in the Okura laboratory contained 12.8 copper ions per 326 kDa complex (*37, 38*).

Table 3: Specific Activity of *M. trichosporium* OB3b pMMO

	reductant	specific activity [nmol of propylene oxidized·min^{-1}·(mg of protein)$^{-1}$]
membrane-bound	NADH	2.9 ± 1.7
	duroquinol	3.0 ± 0.5
solubilized	duroquinol	2.91 ± 0.4
purified	duroquinol	0.11 ± 0.1

This value was later revised to 2 copper ions per 94 kDa complex (*7*). The latter value is consistent with the current data as well as most reports for purified *M. capsulatus* (Bath) pMMO (*4–6*). In our experience, copper in *M. trichosporium* OB3b pMMO is more labile than that in *M. capsulatus* (Bath) pMMO. The crystallographic data (vide infra) indicate the presence of 3 copper ions per protomer; this discrepancy could be due to selective crystallization of a highly copper loaded population. Membrane-bound, solubilized, and purified *M. trichosporium* OB3b pMMO all contain less than 0.01 iron and zinc ions per protomer (Table 2). This finding is consistent with the absence of iron reported previously by the Okura laboratory; zinc was not measured in this study (*7*). Notably, all preparations of *M. capsulatus* (Bath) pMMO (*4–6, 13*) except those from the Chan laboratory (*7*) contain significant amounts of iron.

The average specific activity of membrane-bound *M. trichosporium* OB3b pMMO is 2.9 ± 1.7 or 3.0 ± 0.5 with NADH or duroquinol as the reductants, respectively (Table 3). These results agree with values of 2−5 reported by Okura and co-workers for membrane-bound *M. trichosporium* OB3b pMMO (*7, 37, 38*). Much higher specific activities have been reported for *M. capsulatus* (Bath) pMMO (*3*), but at this point it is unclear whether similar levels of activity are attainable with the *M. trichosporium* OB3b enzyme. The two organisms grow at different temperatures, the growth condi-

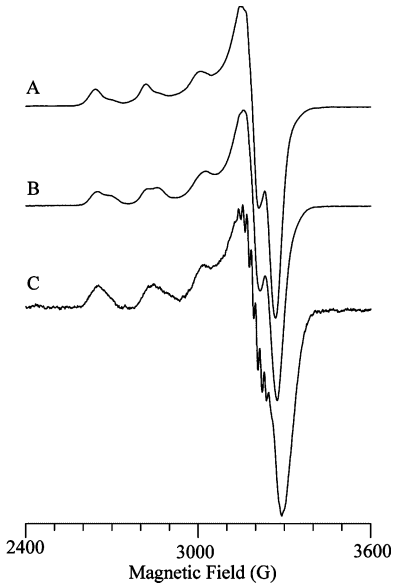

FIGURE 2: X-band EPR spectra of membrane-bound (A), solubilized (B), and purified (C) *M. trichosporium* OB3b pMMO. The spectra have been normalized for easier comparison. Experimental conditions: temperature, 77 K; microwave frequency, 9.21 GHz; microwave power, 7 mW; 100 kHz field modulation amplitude, 5 G; time constant, 300 ms; scan time, 4 min.

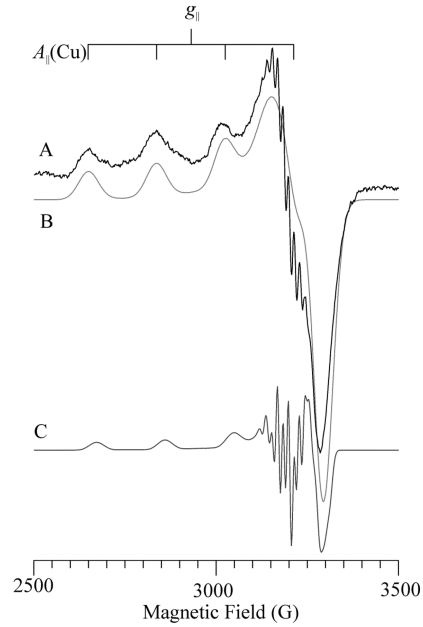

FIGURE 3: X-band EPR of purified *M. trichosporium* OB3b pMMO. (A) The experimental spectrum. (B) The simulation of the major component with parameters: $g_{\perp} = 2.052$, $g_{||} = 2.247$, $A(^{63}Cu)_{||} = 585$ MHz, $A(^{63}Cu)_{\perp} = 60$ MHz (this last value has significant uncertainty); Gaussian line shapes are used with single-crystal line widths of 100 MHz (half-width at half-maximum). (C) The simulation of the minor component with parameters: $g_{\perp} = 2.060$, $g_{||} = 2.225$, $A(^{63}Cu)_{||} = 585$ MHz, $A(^{63}Cu)_{\perp} = 60$ MHz (both ^{63}Cu hyperfine couplings are set equal to the values determined for the major component) and with hyperfine couplings to two equivalent nitrogen nuclei: $A(^{14}N)_{isotropic} = 40$ MHz; line widths are 18 MHz at $g_{\perp}$ and 40 MHz at $g_{||}$. The relative intensities of the two have been scaled to approximate their relative amounts, but precise quantitation is not implied.

tions and growth rates vary (*39*), and it is well documented that the specific activities of sMMO purified from *M. capsulatus* (Bath) (*40*) and *M. trichosporium* OB3b (*41*) are different despite having virtually identical active sites. Addition of 100 μM $CuSO_4$, $Fe(NH_4)SO_4$, or $ZnSO_4$ to the assay mixture does not substantially improve activity. The Okura laboratory has reported that copper addition up to ~100 μM increases activity (*37*), but those experiments utilized cells grown at 10 μM copper whereas our media contains 50 μM copper, which may be sufficient to load all the copper sites. Unlike *M. capsulatus* (Bath) pMMO (*6*), solubilization with DDM does not appreciably decrease activity. After purification, *M. trichosporium* OB3b pMMO exhibits decreased activity of 0.11 ± 0.01 (Table 3). Comparable values of 0.5−3.5 have been reported previously (*7, 38*). Similar to results reported by Okura and coworkers, a neutral pH (*37*) and the use of Brij-58 detergent (*38*) were crucial for observing activity in purified pMMO.

EPR Spectroscopy. The X-band EPR spectra of membrane-bound, solubilized, and purified *M. trichosporium* OB3b pMMO are shown in Figure 2. All forms of the enzyme are heterogeneous by EPR with at least two types of closely related mononuclear type 2 Cu(II) signals. For membrane-bound and solubilized pMMO, no hyperfine coupling from nuclei other than $^{63,65}Cu$ is observable. However, the X-band EPR spectrum of purified pMMO exhibits resolved hyperfine coupling that can be assigned to that from ^{14}N nuclei. The two overlaid signals (Figure 3) in purified pMMO can be described by the following parameters: a major component with $g_{\perp} = 2.052$, $g_{||} = 2.247$, $A(^{63}Cu)_{||} = 585$ MHz, $A(^{63}Cu)_{\perp} = 60$ MHz (this last value has significant uncertainty) and a minor component with $g_{\perp} = 2.060$, $g_{||} = 2.225$, and with ^{63}Cu hyperfine coupling indistinguishable from that of the major component, but with hyperfine coupling of about 40 MHz to two equivalent nitrogen nuclei. Due to the uncertainty in the EPR parameters in the perpendicular region, which dominates the overall integrated signal intensity of the components, we cannot precisely quantify the relative amount of the two components beyond estimating that the major component is at least 80% of the total signal. Because of spectral overlap, it is possible that as many as three nitrogen nuclei are coupled, but on the basis of the crystallographic data (ref *14* and vide infra), two nitrogen ligands are reasonable.

These spectra are similar to those reported previously for pMMOs from *M. capsulatus* (Bath), *Methylomicrobium album* BG8, and *M. trichosporium* OB3b (*4–6, 12, 42*). The $g_{||}$ value for the minor component is smaller than other reported parameters and could be indicative of a site slightly different from those seen in other pMMO preparations. The well-resolved hyperfine lines associated with the second, minor component are also observed in whole cell samples of *M. capsulatus* (Bath) and *M. album* BG8 pMMOs (*12*). Integration relative to a Cu(II) standard indicates that ~85% of the total copper in the sample is EPR active, in contrast to the 40−60% EPR active copper observed for the *M. capsulatus* (Bath) enzyme (*4, 6*). This difference may be related to the lower copper stoichiometry in *M. trichosporium* OB3b pMMO. If the dicopper center (vide infra) is not fully occupied, a larger amount of Cu(II) would be detected by EPR. Importantly, no signal attributable to a trinuclear copper center (*11, 43*) is detected. Although initial EPR spectra from the Okura group supported the presence of a tricopper center in *M. trichosporium* OB3b pMMO (*37, 38*), the signal was not detected once the purification was optimized (*7*), consistent with the current results.

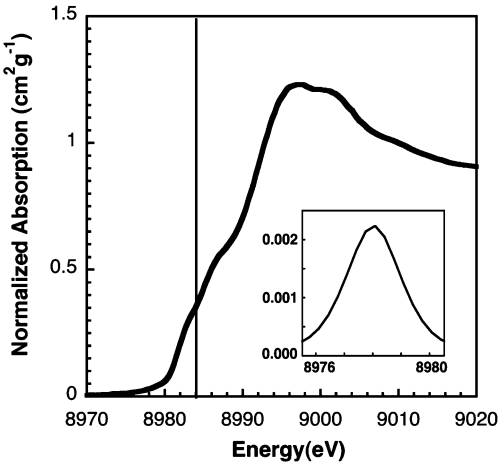

FIGURE 4: Copper XANES spectrum of purified *M. trichosporium* OB3b pMMO. The solid vertical line at 8984 eV identifies spectral features corresponding to the Cu(I) 1s → 4p transition, and the inset shows an expanded view of the Cu(II) 1s → 3d transition.

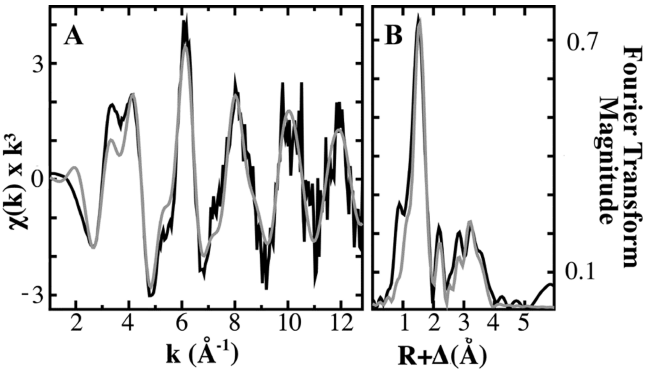

FIGURE 5: Copper EXAFS fitting analysis for purified *M. trichosporium* OB3b pMMO. (A) Raw unfiltered EXAFS data (black) and simulations (gray) for copper bound to pMMO. (B) Fourier transforms of the raw EXAFS (black) and best-fit simulation (gray).

XAS Spectroscopy. The copper K-edge XAS near edge spectrum of purified *M. trichosporium* OB3b pMMO (Figure 4) shows pre-edge features centered at 8980 and 8984 eV. The absorption feature at 8980 eV, attributed to a 1s → 3d transition for centrosymmetric Cu(II), has a low area of 0.52 (unitless) indicating that copper is partially present as Cu(I). The feature at 8984 eV, characteristic of a Cu(I) 1s → 4p transition, is also observable but weak. These results indicate that the copper in this sample is a mixture of Cu(I) and Cu(II) (*44*).

Copper bound to pMMO has an averaged nearest neighbor coordination environment constructed of nitrogen, oxygen, and copper ligands. Raw EXAFS for a representative data set shows a camel-back beat pattern at $k \sim 3.8$ Å^{-1}, characteristic of histidine imidazole multiple scattering (*45*), and a weakly defined node in the data at $k \sim 9$ Å^{-1} (Figure 5A). The Fourier transform of the Cu EXAFS (Figure 5B) shows two peaks below the bond length shifted value of 2.6 Å, indicative of two distinct nearest neighbor environments, as well as long-range scattering at $R > 3.0$ Å. EXAFS simulations indicate the average Cu nearest neighbor environment is constructed of oxygen/nitrogen ligands at 1.97 Å and distinct Cu−Cu coordination at 2.52 Å (Table 4). Attempts to include sulfur scattering were unsupported by these data. Long-range scattering ($R > 3$ Å) could be best fit with carbon scattering at 3.02 and 3.94 Å (Table 4, fit 4), suggestive of histidine imidazole scattering. However, although we were able to simulate the Cu EXAFS using a multiple scattering Cu−imidazole theoretical model (Table 4, fit 5), this simulation gave coordination parameters that were not justified based on an elevated degrees of freedom weighed goodness of fit (F') parameter as well as resolvable bond lengths based on the resolution of the data. Therefore, fits using the single scattering models gave the best fit simulation (Table 4, fit 4). These results are nearly identical to the average oxygen/nitrogen distance of 1.97 Å and Cu−Cu distance of 2.51 Å obtained for as-isolated, purified *M. capsulatus* (Bath) pMMO (*24*). The observation of a short Cu−Cu interaction in pMMO from a second organism strengthens the previous EXAFS results on *M. capsulatus* (Bath) pMMO (*24*) and strongly supports the presence and functional relevance of the dicopper center modeled in the *M. capsulatus* (Bath) pMMO structure (*14*).

Crystal Structure. The crystal structure of *M. trichosporium* OB3b was solved to 3.9 Å resolution, with some information also obtained from incomplete anisotropic data to 2.9 Å resolution (Table 1). Despite exhaustive efforts, the resolution could not be improved. Nevertheless, information about the overall structure and critical new insight into the metal centers has been obtained. The overall architecture of the enzyme is the same as *M. capsulatus* (Bath) pMMO (*14, 15*), an $\alpha_3\beta_3\gamma_3$ trimer. Each protomer has a soluble region composed of two cupredoxin-like β barrels and a transmembrane region that includes 15 α helices as compared to 14 α helices in the *M. capsulatus* (Bath) model. Clear density for an additional helix is apparent in each protomer near the first two helices of the pmoC subunit (Figure 6). Modeling of a polyalanine helix in this density significantly decreased the R_{free} value, although the sequence of this helix could not be determined at 3.9 Å resolution or using the anisotropically processed data (Table 1). One candidate for the sequence is the N-terminal 17 residues of the pmoC subunit, which are not present elsewhere in the model. However, this sequence is not predicted to be a transmembrane helix by the TMHMM server at the Center for Biological Sequence Analysis (http://www.cbs.dtu.dk/services/TMHMM/). Additional residues at the C-terminus of pmoC are also unmodeled, but if these residues are present in this helix, it is unclear how to connect the backbone to the rest of the subunit. Besides this extra helix, a helix near the C-terminal part of pmoC has been modified in the *M. trichosporium* OB3b structure. In the *M. capsulatus* (Bath) structure, residues 231−259 are modeled as a helix disconnected from the rest of pmoC (*14*). The N-terminus of this helix is on the side of pMMO opposite the soluble cupredoxin domains, and its C-terminus is in the membrane. Analysis of this sequence for both pMMOs using the TMHMM server reveals that this helix most likely runs in the opposite direction. Its orientation was therefore reversed in the current structure, although it was modeled as polyalanine due to poor density in this area, and was also shortened due to a lack of density at end furthest from the soluble region.

Although the resolution is not sufficient to obtain details regarding metal coordination, anomalous data collected at different wavelengths provide new insight into the location and identity of the metal ions in the structure. Anomalous Fourier maps calculated using data collected just above the

Table 4: Summary of Cu EXAFS Fitting Analysis for *M. trichosporium* OB3b pMMO[a]

	ligand environment[b]				ligand environment[b]				ligand environment[b]				
fit	atom[c]	*R* (Å)[d]	CN[e]	σ^2 [f]	atom[c]	*R* (Å)[d]	CN[e]	σ^2 [f]	atom[c]	*R* (Å)[d]	CN[e]	σ^2 [f]	*F*′ [g]
1[h]	O/N	1.97	2.0	3.51									0.58
2[h]	O/N	1.97	2.0	3.54	Cu	2.52	0.5	4.56					0.54
3[h]	O/N	1.97	2.0	3.52	Cu	2.52	0.5	4.22	C	3.02	3.0	4.95	0.41
4[h]	**O/N**	**1.97**	**2.0**	**3.60**	**Cu**	**2.52**	**0.5**	**4.30**	**C**	**3.02**	**2.0**	**4.30**	**0.36**
									C	**3.94**	**4.0**	**4.54**	
5[i]	N_{im}	2.01	2.0	4.41	Cu	2.52	0.5	5.41					0.44
	O/N	1.99	1.5	4.82									

[a] Data fit over a *k* range of 1−12.85 Å^{-1}. Best-fit parameters are indicated in bold. [b] Independent metal−ligand scattering environment. [c] Scattering atoms: O (oxygen), N (nitrogen), C (carbon), and Cu (copper). [d] Average metal−ligand bond length for two independent samples. [e] Average metal−ligand coordination number for two independent samples. [f] Average Debye−Waller factor in Å^2 × 10 (*3*) for two independent samples. [g] Number of degrees of freedom weighted mean square deviation between data and fit. [h] Fit using only single scattering Feff 8 theoretical models. [i] Fit using both single scattering Feff 8 model with an additional multiple scattering Cu−N(imidazole) model, generated based on crystallographic coordinates, and labeled N_{Im} in table atom designation.

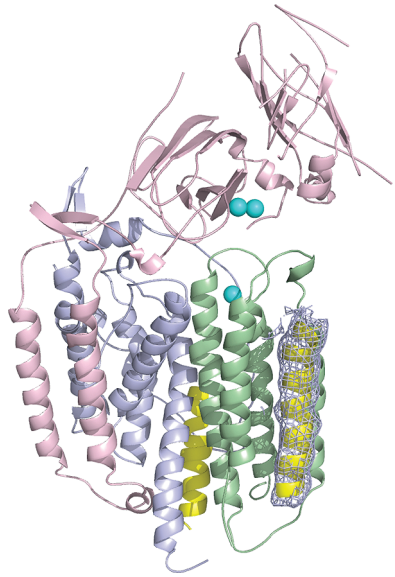

FIGURE 6: Crystal structure of *M. trichosporium* OB3b pMMO protomer with pmoB shown in pink, pmoA in light blue, and pmoC in light green. Modeled copper ions are shown as cyan spheres. Two helices in pmoC that differ from the *M. capsulatus* (Bath) structure are shown in yellow. The helix in front, which is not present in the *M. capsulatus* (Bath) structure, is shown with the $2F_o - F_c$ electron density superimposed at 1σ. The direction of the yellow helix in back has been reversed with respect to the *M. capsulatus* (Bath) pMMO structure.

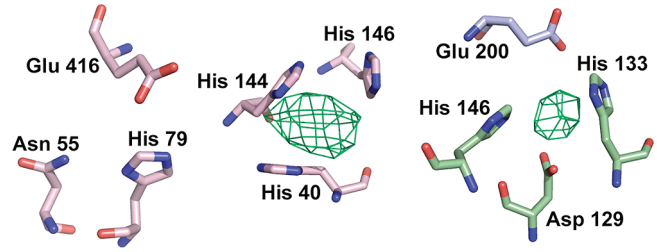

FIGURE 7: Copper anomalous difference Fourier maps of the three metal centers in *M. trichosporium* OB3b pMMO. Left: The location of the monocopper center in *M. capsulatus* (Bath) pMMO. No anomalous density is observed. Middle: The location of the dicopper center in *M. capsulatus* (Bath) pMMO with the anomalous map contoured at 4σ. Right: The location of the "zinc" center *M. capsulatus* (Bath) pMMO with the anomalous map contoured at 3σ. Side chain positions are not well defined at this resolution, and details of coordination cannot be acsertained. Oxygen atoms are colored red, nitrogen atoms are colored blue, and carbon atoms are colored according to subunit as in Figure 6.

Cu absorption edge (Table 1) reveal strong, oblong density in the site modeled as a dicopper center in *M. capsulatus* (Bath) pMMO (Figure 7). This density, combined with the EXAFS data (Table 4 and Figure 5), strongly suggests that the dicopper center is present in *M. trichosporium* OB3b pMMO as well. Whether this dicopper center is the active site remains unknown, but its existence in pMMO from two different organisms is consistent with an important functional role. By contrast, the Cu anomalous map is devoid of density at the site occupied by the mononuclear copper center in *M. capsulatus* (Bath) pMMO (Figure 7). The lack of density at this location is consistent with the replacement of one histidine with an asparagine in the *M. trichosporium* OB3b sequence, and it is therefore unlikely that this site is absolutely necessary for function. There is also no density in the Cu anomalous maps at a hydrophilic site within the membrane proposed to house a trinuclear copper center (*10*).

Most striking, Cu anomalous density is also observed in the site occupied by zinc in the *M. capsulatus* (Bath) structure (Figure 7), the so-called "zinc site". For *M. capsulatus* (Bath) pMMO, no density was apparent at this site in Cu anomalous maps (*14*). Therefore, it seems likely that copper in this site was displaced by the high concentration of zinc used to crystallize *M. capsulatus* (Bath) pMMO. In the case of *M. trichosporium* OB3b pMMO, zinc was not necessary for crystallization. Neither purified enzyme contains zinc (ref *14* and Table 2). Data nevertheless were collected near the Zn absorption edge, and features in the Zn anomalous map overlap with those in the Cu anomalous map as expected since the Zn edge is at higher energy. There are no features in the Zn anomalous map that are not observed in the Cu anomalous map, consistent with the absence of zinc in purified *M. trichosporium* OB3b pMMO. The "zinc site" has been proposed to house a diiron center (*14, 16*). Metal analysis (Table 2) and X-ray fluorescence scans of crystals provide no evidence for iron in *M. trichosporium* OB3b pMMO. The current data are consistent with copper occupying the "zinc site," but it is also possible that iron originally at this site could have been depleted during purification and/or crystallization and replaced with copper. However, even membrane-bound *M. trichosporium* OB3b pMMO has very little iron (Table 2) despite the presence of 40 μM iron in the growth medium.

In sum, EXAFS and crystallographic data provide strong evidence that *M. trichosporium* OB3b pMMO contains a dicopper center similar to that found in *M. capsulatus* (Bath) pMMO. The *M. capsulatus* (Bath) "zinc site" appears to

house a copper ion in *M. trichosporium* OB3b pMMO, suggesting that copper may be the physiological metal ion at this conserved site. No metal ions are detected at the location of the *M. capsulatus* (Bath) monocopper center, eliminating the possibility of a functionally essential site at this position. EPR data indicate the presence of nitrogen-ligated type 2 Cu(II), which could derive from the copper in the "zinc site" or from the dicopper center if it exists as a trapped valence Cu(I)Cu(II) site (*46*) or from both sites. There is no indication of a trinuclear copper cluster in *M. trichosporium* OB3b pMMO, and the copper stoichiometry is not consistent with multiple tricopper centers as proposed previously (*11*). Taken together with previous work, the characterization of *M. trichosporium* OB3b pMMO provides new insight into the metal centers and represents a significant step toward elucidating the active site.

ACKNOWLEDGMENT

GM/CA CAT has been funded in whole or in part with Federal funds from the National Cancer Institute (Y1-CO-1020) and the National Institute of General Medical Science (Y1-GM-1104). Use of the Advanced Photon Source was supported by the U.S. Department of Energy, Basic Energy Sciences, Office of Science, under Contract No. DE-AC02-06CH11357. SSRL is a national user facility operated by Stanford University on behalf of the U.S. Department of Energy, Office of Basic Energy Sciences. The SSRL Structural Molecular Biology Program is supported by the Department of Energy, Office of Biological and Environmental Research, and by the NIH, National Center for Research Resources, Biomedical Technology Program. NSLS, located at Brookhaven National Laboratory, is supported by the U.S. Department of Energy, Division of Materials Sciences and Division of Chemical Sciences, under Contract No. DE-AC02-98CH10886. ICP-OES measurements were performed at the Northwestern University Analytical Services Laboratory. A description of the facility and full funding disclosure can be found at http://pyrite.chem.northwestern-.edu/analyticalserviceslab/asl.htm.

REFERENCES

1. Hanson, R. S., and Hanson, T. E. (1996) Methanotrophic bacteria. *Microbiol. Rev. 60*, 439–471.
2. Merkx, M., Kopp, D. A., Sazinsky, M. H., Blazyk, J. L., Müller, J., and Lippard, S. J. (2001) Dioxygen activation and methane hydroxylation by soluble methane monooxygenase: a tale of two irons and three proteins. *Angew. Chem., Int. Ed. 40*, 2782–2807.
3. Hakemian, A. S., and Rosenzweig, A. C. (2007) The biochemistry of methane oxidation. *Annu. Rev. Biochem. 76*, 223–241.
4. Basu, P., Katterle, B., Andersson, K. K., and Dalton, H. (2003) The membrane-associated form of methane monooxygenase from *Methylococcus capsulatus* (Bath) is a copper/iron protein. *Biochem. J. 369*, 417–427.
5. Choi, D. W., Kunz, R. C., Boyd, E. S., Semrau, J. D., Antholine, W. E., Han, J. I., Zahn, J. A., Boyd, J. M., de la Mora, A. M., and DiSpirito, A. A. (2003) The membrane-associated methane monooxygenase pMMO and pMMO-NADH:quinone oxidoreductase complex from *Methylococcus capsulatus* Bath. *J. Bacteriol. 185*, 5755–5764.
6. Lieberman, R. L., Shrestha, D. B., Doan, P. E., Hoffman, B. M., Stemmler, T. L., and Rosenzweig, A. C. (2003) Purified particulate methane monooxygenase from *Methylococcus capsulatus* (Bath) is a dimer with both mononuclear copper and a copper-containing cluster. *Proc. Natl. Acad. Sci. U.S.A. 100*, 3820–3825.
7. Miyaji, A., Kamachi, T., and Okura, I. (2002) Improvement of the purification method for retaining the activity of the particulate methane monooxygenase from *Methylosinus trichosporium* OB3b. *Biotechnol. Lett. 24*, 1883–1887.
8. Nguyen, H. H., Elliott, S. J., Yip, J. H., and Chan, S. I. (1998) The particulate methane monooxygenase from *Methylococcus capsulatus* (Bath) is a novel copper-containing three-subunit enzyme. Isolation and characterization. *J. Biol. Chem. 273*, 7957–7966.
9. Yu, S. S.-F., Chen, K. H.-C., Tseng, M. Y.-H., Wang, Y.-S., Tseng, C.-F., Chen, Y.-J., Huang, D. S., and Chan, S. I. (2003) Production of high-quality particulate methane monooxygenase in high yields from *Methylococcus capsulatus* (Bath) with a hollow-fiber membrane bioreactor. *J. Bacteriol. 185*, 5915–5924.
10. Chan, S. I., Wang, V. C. C., Lai, J. C. H., Yu, S. S. F., Chen, P. P. Y., Chen, K. H. C., Chen, C. L., and Chan, M. K. (2007) Redox potentiometry studies of particulate methane monooxygenase: support for a trinuclear copper cluster active site. *Angew. Chem., Int. Ed. 46*, 1992–1994.
11. Hung, S.-C., Chen, C.-L., Chen, K. H.-C., Yu, S. S.-F., and Chan, S. I. (2004) The catalytic copper clusters of the particulate methane monooxygenase from methanotropic bacteria: electron paramagnetic resonance spectral simulations. *J. Chin. Chem. Soc. 51*, 1229–1244.
12. Lemos, S. S., Collins, M. L. P., Eaton, S. S., Eaton, G. R., and Antholine, W. E. (2000) Comparison of EPR-visible Cu^{2+} sites in pMMO from *Methlococcus capsulatus* (Bath) and *Methlyomicrobium album* BG8. *Biophys. J. 79*, 1085–1094.
13. Zahn, J. A., and DiSpirito, A. A. (1996) Membrane-associated methane monooxygenase from *Methylococcus capsulatus* (Bath). *J. Bacteriol. 178*, 1018–1029.
14. Lieberman, R. L., and Rosenzweig, A. C. (2005) Crystal structure of a membrane-bound metalloenzyme that catalyzes the biological oxidation of methane. *Nature 434*, 177–182.
15. Lieberman, R. L., and Rosenzweig, A. C. (2005) The quest for the particulate methane monooxygenase active site. *Dalton Trans. 21*, 3390–3396.
16. Martinho, M., Choi, D. W., DiSpirito, A. A., Antholine, W. E., Semrau, J. D., and Münck, E. (2007) Mössbauer studies of the membrane-associated methane monooxygenase from *Methylococcus capsulatus* Bath: evidence for a diiron center. *J. Am. Chem. Soc. 129*, 15783–15785.
17. Fox, B. G., Froland, W. A., Jollie, D. R., and Lipscomb, J. D. (1990) Methane Monooxygenase from *Methylosinus trichosporium* OB3b. *Methods Enzymol. 188*, 191–202.
18. Colby, J., Stirling, D. I., and Dalton, H. (1977) The soluble methane monooxygenase of *Methylococcus capsulatus* (Bath). Its ability to oxygenate n-alkanes, ethers, and alicyclic, aromatic and heterocyclic compounds. *Biochem. J. 165*, 395–402.
19. Belford, R. L., and Belford, G. G. (1973) Eigenfield expansion technique for efficient computation of field-swept fixed-frequency spectra from relaxation master equations. *J. Chem. Phys. 59*, 853–854.
20. Belford, R. L., and Nilges, M. J. (1979) EPR Symposium, 21st Rocky Mountain Conference, Denver, CO.
21. George, G. N., George, S. J., and Pickering, I. J. (2001) http://www-ssrl.slac.stanford.edu/~george/exafspak/exafs.htm.
22. Ankudinov, A. L., and Rehr, J. J. (1997) Relativistic calculations of spin-dependent X-ray absorption spectra. *Phys. Rev. B 56*, R1712–R1715.
23. Lee, P. A., Citrin, P. H., Eisenberger, P., and Kincaid, B. M. (1981) Extended x-ray absorption fine structure—its strengths and limitations as a structural tool. *Rev. Mod. Phys. 53*, 769–806.
24. Lieberman, R. L., Kondapalli, K. C., Shrestha, D. B., Hakemian, A. S., Smith, S. M., Telser, J., Kuzelka, J., Gupta, R., Borovik, A. S., Lippard, S. J., Hoffman, B. M., Rosenzweig, A. C., and Stemmler, T. L. (2006) Characterization of the particulate methane monooxygenase metal centers in multiple redox states by X-ray absorption spectroscopy. *Inorg. Chem. 45*, 8372–8381.
25. Bencze, K. Z., Kondapalli, K. C., and Stemmler, T. L. (2007) X-ray absorption spectroscopy, in *Applications of Physical Methods to Inorganic and Bioinorganic Chemistry: Handbook, Encyolopedia of Inorganic Chemistry* (Scott, R. A., and Lukehart, C. M., Eds.) pp 513−528, John Wiley & Sons, Chichester, U.K.
26. Kabsch, W. (1993) Automatic processing of rotation diffraction data from crystals of initially unknown symmetry and cell constants. *J. Appl. Crystallogr. 26*, 795–800.
27. Leslie, A. G. W. (1992) Recent changes to the MOSFLM package for processing film and image plate data, Joint CCP4 + ESF-EAMCB Newsletter on Protein Crystallography 26.

28. Collaborative Computational Project (1994) The CCP4 suite programs for protein crystallography, *Acta Crystallogr. D50*, 760−763.
29. McCoy, A. J., Grosse-Kunstleve, R. W., Storoni, L. C., and Read, R. J. (2005) Likelihood-enhanced fast translation functions. *Acta Crystallogr. D61*, 458–464.
30. Guex, N., and Peitsch, M. C. (1997) SWISS-MODEL and the Swiss-PdbViewer: an environment for comparative protein modeling. *Electrophoresis 18*, 2714–2723.
31. Emsley, P., and Cowtan, K. (2004) Coot: model-building tools for molecular graphics. *Acta Crystallogr. D60*, 2126–2132.
32. Brünger, A. T., Adams, P. D., Clore, G. M., DeLano, W. L., Gros, P., Grosse-Kunstleve, R. W., Jiang, J.-S., Kuszewski, J., Nilges, M., Pannu, N. S., Read, R. J., Rice, L. M., Simonson, T., and Warren, G. L. (1998) *Crystallography & NMR system*: a new software suite for macromolecular crystallography. *Acta Crystallogr. D54*, 905–921.
33. Strong, M., Sawaya, M. R., Wang, S., Phillips, M., Cascio, D., and Eisenberg, D. (2006) Toward the structural genomics of complexes: crystal structure of a PE/PPE protein complex from *Mycobacterium tuberculosis*. *Proc. Natl. Acad. Sci. U.S.A. 103*, 8060–8065.
34. Laskowski, R. A. (1993) *PROCHECK*: a program to check the stereochemical quality of protein structures. *J. Appl. Crystallogr. 26*, 283–291.
35. Lieberman, R. L., and Rosenzweig, A. C. (2004) Biological methane oxidation: regulation, biochemistry, and active site structure of particulate methane monooxygenase. *Crit. Rev. Biochem. Mol. Biol. 39*, 147–164.
36. Takeguchi, M., Miyakawa, K., and Okura, I. (1999) The role of copper in particulate methane monooxygenase from *Methylosinus trichosporium* OB3b. *J. Mol. Catal. A 137*, 161–168.
37. Takeguchi, M., and Okura, I. (2000) Role of iron and copper in particulate methane monooxygenase of *Methylosinus trichosporium* OB3b. *Catal. Surv. Jpn. 4*, 51–63.
38. Takeguchi, M., Miyakawa, K., and Okura, I. (1998) Purification and properties of particulate methane monooxygenase from *Methylosinus trichosporium* OB3b. *J. Mol. Catal. A 132*, 145–153.
39. Whittenbury, R., Phillips, K. C., and Wilkinson, J. F. (1970) Enrichment, isolation and some properties of methane-utilizing bacteria. *J. Gen. Microbiol. 61*, 205–218.
40. DeWitt, J. G., Bentsen, J. G., Rosenzweig, A. C., Hedman, B., Green, J., Pilkington, S., Papaefthymiou, G. C., Dalton, H., Hodgson, K. O., and Lippard, S. J. (1991) X-ray absorption, mössbauer, and EPR studies of the dinuclear iron center in the hydroxylase component of methane monooxygenase. *J. Am. Chem. Soc. 113*, 9219–9235.
41. Fox, B. G., Froland, W. A., Dege, J. E., and Lipscomb, J. D. (1989) Methane monooxygenase from *Methylosinus trichosporium* OB3b. *J. Biol. Chem. 264*, 10023–10033.
42. Zahn, J. A., Arciero, D. M., Hooper, A. B., and Dispirito, A. A. (1996) Evidence for an iron center in the ammonia monooxygenase from *Nitrosomonas europaea*. *FEB Lett. 397*, 35–38.
43. Chen, K. H.-C., Chen, C.-L., Tseng, C.-F., Yu, S. S.-F., Ke, S.-C., Lee, J.-F., Nguyen, H. T., Elliott, S. J., Alben, J. O., and Chan, S. I. (2004) The copper clusters in the particulate methane monooxygenase (pMMO) from *Methylococcus capsulatus* (Bath). *J. Chin. Chem. Soc. 51*, 1081–1098.
44. Kau, L.-S., Spira-Solomon, D. J., Penner-Hahn, J. E., Hodgson, K. O., and Solomon, E. I. (1987) X-ray absorption edge determination of the oxidation state and coordination number of copper. Application to the type 3 site in *Rhus vernicifera* laccase and its reaction with oxygen. *J. Am. Chem. Soc. 109*, 6433–6442.
45. Wang, S., Lee, M. H., Hausinger, R. P., Clark, P. A., Wilcox, D. E., and Scott, R. A. (1994) Structure of the dinuclear active site of urease. X-ray absorption spectroscopic study of native and 2-mercaptoethanol-inhibited bacterial and plant enzymes. *Inorg. Chem. 33*, 1589–1593.
46. Balasubramanian, R., and Rosenzweig, A. C. (2007) Structural and mechanistic insights into methane oxidation by particulate methane monooxygenase. *Acc. Chem. Res. 40*, 573–580.

BI800598H